Ultra-wideband signal acquisition by use of channel-interleaved photonic analog-to-digital converter under the assistance of dilated fully convolutional network

Rui Wang (汪 锐), Shaofu Xu (徐绍夫), Jianping Chen (陈建平), and Weiwen Zou (邹卫文)*

State Key Laboratory of Advanced Optical Communication Systems and Networks, Intelligent Microwave Lightwave Integration Innovation Center (iMLic), Department of Electronic Engineering, Shanghai Jiao Tong University, Shanghai 200240, China

**Corresponding author: wzou@sjtu.edu.cn*

Received June 28, 2020; accepted August 11, 2020; posted online September 28, 2020

We demonstrate a photonic architecture to enable the separation of ultra-wideband signals. The architecture consists of a channel-interleaved photonic analog-to-digital converter (PADC) and a dilated fully convolutional network (DFCN). The aim of the PADC is to perform ultra-wideband signal acquisition, which introduces the mixing of signals between different frequency bands. To alleviate the interference among wideband signals, the DFCN is applied to reconstruct the waveform of the target signal from the ultra-wideband mixed signals in the time domain. The channel-interleaved PADC provides a wide spectrum reception capability. Relying on the DFCN reconstruction algorithm, the ultra-wideband signals, which are originally mixed up, are effectively separated. Additionally, experimental results show that the DFCN reconstruction algorithm improves the average bit error rate by nearly three orders of magnitude compared with that without the algorithm.

Keywords: ultra-wideband signal acquisition; photonic analog-to-digital converter; deep learning.
doi: 10.3788/COL202018.123901.

A wide operating frequency range and sufficient instantaneous receiving bandwidth are indispensable for signal reconnaissance, which is one of the key technologies of electronic warfare (EW)[1,2]. Conventional reconnaissance equipment is faced with a great challenge with the development of modern electronic information technology. The introduction of photonic technology provides a new idea for the research and development of reconnaissance equipment. A photonic analog-to-digital converter (PADC) combines the advantages of the optical front end, namely high speed, low jitter, and wide bandwidth, with the characteristic of high accuracy of the electronic back end. Thus, it improves system performance and provides an ideal solution for the next-generation information systems[3–8]. Especially in recent years, channel-interleaved PADCs have made tremendous breakthroughs[9–12].

PADC-based systems are of wide receiving bandwidth, which also brings about issues such as more complexity in received signals and severe interference among signals. In this sense, the difficulty of analyzing signals increases, especially when the spectrum of signals is aliased. In order to avoid the influence of interference between signals and accurately extract the signal that we are interested in from the mixture containing multiple signals, the problem is regarded as a single channel blind source separation (SCBSS)[13], of which the purpose is to restore the original source signal from one sensor through various means. To effectively achieve SCBSS, different methods based on hand-crafted algorithms are reported[14–16]. Recently, deep learning[17] has achieved outstanding performance in medical imaging, communication, speech enhancement, and image processing[18–21]. By introducing deep learning technology into the traditional processing systems, superior performance is expected and demonstrated, such as combining optical microscopy with a generative adversarial network (GAN) to achieve super-resolution under a large field of view[22], combining microscope hardware with deep learning to offer accurate image classification[23], and using a residual-on-residual learning model to realize linearization and mismatch compensation in PADC[10].

In this Letter, a channel-interleaved PADC is seamlessly combined with a dilated fully convolutional network (DFCN), which are two essential parts for ultra-wideband signals acquisition. The bandwidth advantage of the PADC is exploited to obtain ultra-wideband signals with a wide operating frequency range and sufficient instantaneous receiving bandwidth [tens of gigahertz (GHz)]. The DFCN successfully separates the target signal from the mixture with high fidelity, lowering the interference among aliased signals. To demonstrate the feasibility of the proposal, several categories of microwave signals are experimentally conducted and separated. Additionally, we implement the signal separation for digitally modulated signals. Experimental results show that our scheme can accurately separate the digital signal under the interference of microwave signals. The average bit error rate (BER) has been improved by about three orders of magnitude after separation of the digital signal.

Figure 1 shows the model for ultra-wideband signals acquisition and separation, which is mainly composed of two

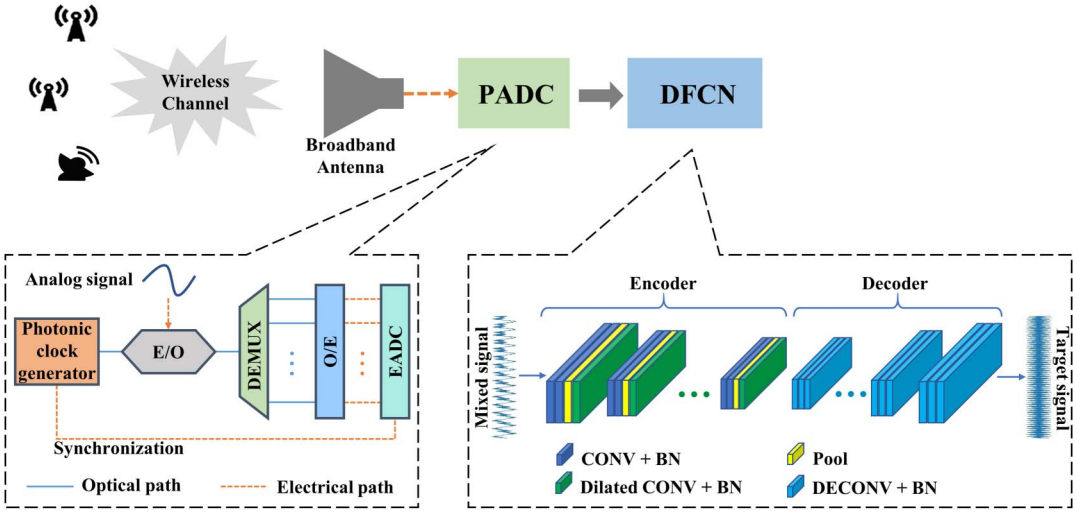

Fig. 1. Schematic of proposed ultra-wideband signal acquisition architecture. The architecture is mainly composed of two parts: a channel-interleaved photonic analog-to-digital converter (PADC) and a dilated fully convolutional network (DFCN). E/O, electro-optical modulation; DEMUX, demultiplexer; O/E, optical-electronic conversion; EADC, electronic analog-to-digital converter; CONV, convolution; BN, batch normalization; DECONV, deconvolution.

parts: a channel-interleaved PADC and a back-end artificial neural network, namely the DFCN. The channel-interleaved PADC converts wideband analog signals into digital signals that can be flexibly processed. The wideband signal is considered as a combination of the target signal and the interference signals. The DFCN separates the target signal from the mixture. As shown in Fig. 1, the analog signal in the channel-interleaved PADC is sampled at a sampling rate of f_s by electronic-optical (E/O) modulation. Then, the pulse train is demultiplexed into multiple parallel channels via a demultiplexer (DEMUX). Finally, the demultiplexed optical pulse trains are photoelectrically converted by a photodetector (PD) array and digitized by an electronic analog-to-digital converter (EADC) array.

The operations of DFCN are shown in Fig. 1. The DFCN is an encoder–decoder neural network based on fully convolutional networks (FCNs)[24]. The encoder module consists of a series of cascaded convolution blocks, and each block contains two convolution layers, a max-pooling layer, and a dilated convolution layer. Among them, the convolution layer is used to extract the features of the target signal from the mixed input. The pooling layer retains the main features while reducing parameters and calculations, thus avoiding overfitting and improving the generalization ability of the model. Through conventional convolutional operations, the receptive field is severely limited. Since the wideband microwave signals are typically holistic and of high dimensionality, small receptive field fails to cover the complete information of the signals. To broaden the receptive field and further fuse the features of the previous stage, dilated convolution operator (also referred to as convolution with a dilated filter, which can apply the same filter in different ranges with different dilation factors) is adopted rather than expanding the size of convolution kernel and the number of convolution layers, which increases the calculation of the network and causes a tendency of overfitting[25]. Each convolution layer is followed by batch normalization (BN)[26], which can accelerate the training of deep neural networks and regularize the model. As previously done in encoding networks, the decoder consists of several cascaded deconvolution blocks, and each block contains three deconvolution layers followed by BN. The resultant feature maps of the encoder are the input of the decoder. The resolution of the feature map is quite low after a series of convolution operations. It is necessary to restore the original signal size by upsampling. Here, the cascaded deconvolution blocks are used for upsampling. The sizes of the feature maps gradually increase as the dimensions decrease. Finally, the time-domain waveform of the target signal is reconstructed. The detail of the DFCN we implemented is described in Table 1. The activation function of each layer is 'tanh,' which is used to increase the nonlinearity of the neural network model and enhance the expression ability of the neural network model.

In order to demonstrate the feasibility of the proposal, two individual experiments based on the same setup are implemented, as shown in Fig. 2. We first separate several common microwave signals. To train the network, it is necessary to prepare a large dataset comprising pairs of mixed signals and the original wideband signal. We adopt a channel-interleaved PADC to achieve wideband mixed signals acquisition, as shown in Fig. 2. An actively mode-locked laser (AMLL) (Calmar PSL-10-TT) is used to generate an optical sampling pulse. Then, the optical sampling pulse passes through a Mach–Zehnder modulator (MZM, Optilab IMC-1550-20-PM; bandwidth, 20 GHz) and is modulated by the wideband mixed signal. The modulated optical pulse is amplified by a customized erbium-doped fiber amplifier (EDFA; gain, 15 dB). A dual-output MZM (DOMZM, EOSpace AX-1x2-0MSS-20) is used as an

Table 1. Detailed Structure of the DFCN

Block	Encoder					Decoder			
		Filters	Kernel	Stride	Rate		Filters	Kernel	Stride
1	Conv1	16	1×3	1×1	/	Deconv1	256	1×4	1×2
	Conv2	32	1×5	1×2	/	Deconv2	256	1×5	1×2
	Max pool	/	1×5	1×2	/	Deconv3	128	1×3	1×1
	Dilated Conv	32	1×4	/	4				
2	Conv1	64	1×3	1×1	/	Deconv1	128	1×4	1×2
	Conv2	128	1×5	1×2	/	Deconv2	64	1×5	1×2
	Max pool	/	1×5	1×2	/	Deconv3	32	1×3	1×1
	Dilated Conv	128	1×4	/	4				
3	Conv1	256	1×3	1×1	/	Deconv1	32	1×4	1×2
	Conv2	256	1×5	1×2	/	Deconv2	16	1×5	1×2
	Max pool	/	1×5	1×2	/	Deconv3	1	1×3	1×1
	Dilated Conv	256	1×4	/	4				

optical switch, which demultiplexes the optical pulse into two channels. An optical tunable delay line (OTDL, General Photonics VDL-001-15-33; delay range, 0–330 ps) guarantees the DOMZM can accurately achieve the switching effect. The demultiplexed signals are converted into electrical signal by two PDs with a bandwidth of 12 GHz (Discovery Semiconductors DSC50S) and quantized by a real-time oscilloscope (OSC, Keysight MSO804A). A microwave generator (MG, Keysight E8257D) provides a microwave signal of 20 GHz, which is divided into two channels by a power splitter (Talent Microwave RS2W04260-S; frequency range, 0.4–26 GHz). One channel is used to drive the AMLL, and consequently the optical sampling rate is 20 GHz. The other channel transferred to 10 GHz by a frequency divider (FD, RF Bay FPS-2-20) is used as driving signal for the optical switch. Furthermore, we use the 10 MHz reference signal from the MG as the reference clock for the OSC to ensure consistency. An arbitrary waveform generator (AWG, Keysight M8152A) is used to generate 5000 wideband mixed signals containing multiple types: continuous wave (CW), linear frequency modulated (LFM), non-LFM (NLFM), and Costas and Barker-13 codes. The carrier frequency, bandwidth, and normalized amplitude of each signal are randomly generated within 8.2–8.7 GHz, 0.3–1.2 GHz, and 0.5–1, respectively. Each sample in our training set is generated from the combination of multiple randomly selected microwave signals. These wideband mixed signals from the AWG are transmitted in pulses by a transmitting antenna (TA1, A-INFO LB-90-20-C-SF; frequency range, 8.2–12.4 GHz), received by a receiving antenna (RA, A-INFO LB-20180-SF; frequency range, 2–18 GHz), and converted into digital signals by the channel-interleaved PADC. The recorded signals are preprocessed as the training dataset for neural network training. We segment the valid part from the received signal by calculating the cross-correlation function of the ground truth and the output of the OSC. For each sample, we also subtract its mean value to avoid the influence of the DC component. Ninety-eight percent of the produced data are used to train the model and the remaining 2% are used to test our model at the same time.

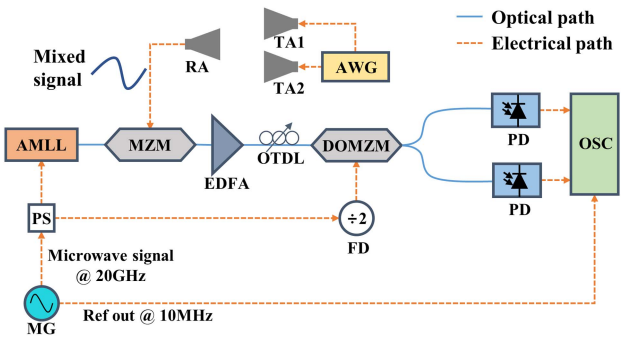

Fig. 2. Experimental setup for the ultra-wideband signal separation architecture. AWG, arbitrary waveform generator; TA, transmitting antenna; RA, receiving antenna; AMLL, actively mode-locked laser; MZM, Mach–Zehnder modulator; EDFA, erbium-doped fiber amplifier; OTDL, optical tunable delay line; DOMZM, dual-output MZM; PD, photodetector; MG, microwave generator; PS, power splitter; FD, frequency divider; OSC, oscilloscope.

To optimize the kernel weights and other network parameters, let x and y denote the input of the network and the ground truth, respectively. Hence, the mean square error (MSE) between the reconstructed signal and the ground truth can be defined as follows:

$$\mathrm{MSE}=\frac{1}{N}\sum_{i=1}^{N}[y_i-f(x_i,\theta)]^2, \tag{1}$$

where f is a model to be learned by minimizing the objective function, and θ is the set of hyper-parameters including weights and biases in our model. We use an 'adam' optimizer with an initial learning rate of 0.001 for back propagation. The whole network is initialized by random weights and biases drawn from Gaussian distributions[27]. We use the TensorFlow software library to train the network over 500 epochs, which takes roughly around 8 h on two NVIDIA GTX 1080Ti 11 GB graphics processing units (GPUs). The entire model is trained end-to-end. Figure 3(a) illustrates the trend of MSE with the growth of epochs. When the epochs are small, the parameter adjustment is still unfinished due to limited iteration times. As the epochs grow, the parameters are further optimized, contributing to the gradually improved performance. After training, all of the parameters of our network are fixed. The DFCN can automatically reconstruct target signals from mixed signals, which are not included in the training set.

The comparison of the time-frequency spectra before and after separation is shown in Figs. 3(b) and 3(c). In addition to the target signal and the generated interference signal, there are some nonlinear components and mismatched components caused by the inherent flaws of the PADC. In recent years, a channel mismatch elimination algorithm based on fractional Fourier domain filtering and an algorithm for channel mismatch compensation in the frequency domain have been proposed and demonstrated[28,29]. Here, the mismatched component is considered as a special interference signal, which is introduced by the channel-interleaved PADC rather than the wireless channel. The mixed signal is input into the DFCN. Through convolution and pooling processing, a series of feature maps are generated. Then, the cascaded deconvolution blocks reconstruction of the target signal according to the feature maps. In order to further compare the difference between the reconstruction results of the network and the ground truth, we calculate the residual between the output of DFCN and the ground truth. It can be seen that the DFCN is able to separate the target signal from the mixture. As shown in Fig. 3(e), although extra nonlinearities are introduced by the neural network, the power of these nonlinearities is minor compared with the reconstructed signal. The quality of the reconstructed signal is characterized by the signal-to-noise ratio (SNR). The SNR is yielded by comparing the ground truth and residual. Figure 4(a) shows the box plot of the SNR of different categories of signals reconstructed by DFCN. It is found that after DFCN reconstruction, the SNR of most signals in the test set exceeds 15 dB. Despite the fact that the SNR of a few reconstruction results is of a low level

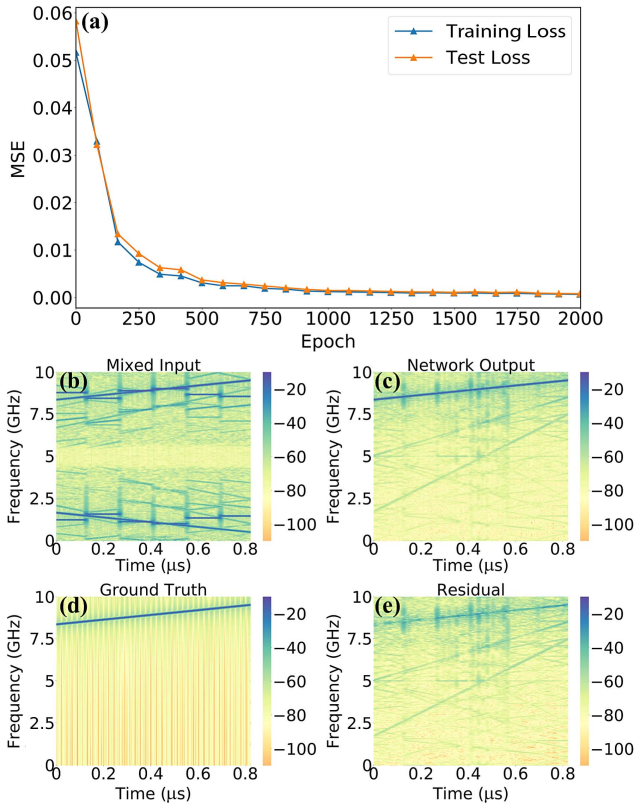

Fig. 3. (a) Training progress of our proposed network. (b), (c) The comparison of the time-frequency spectra before and after separation. (d) Ground truth of the target signal. (e) Residual between the separation result and the ground truth.

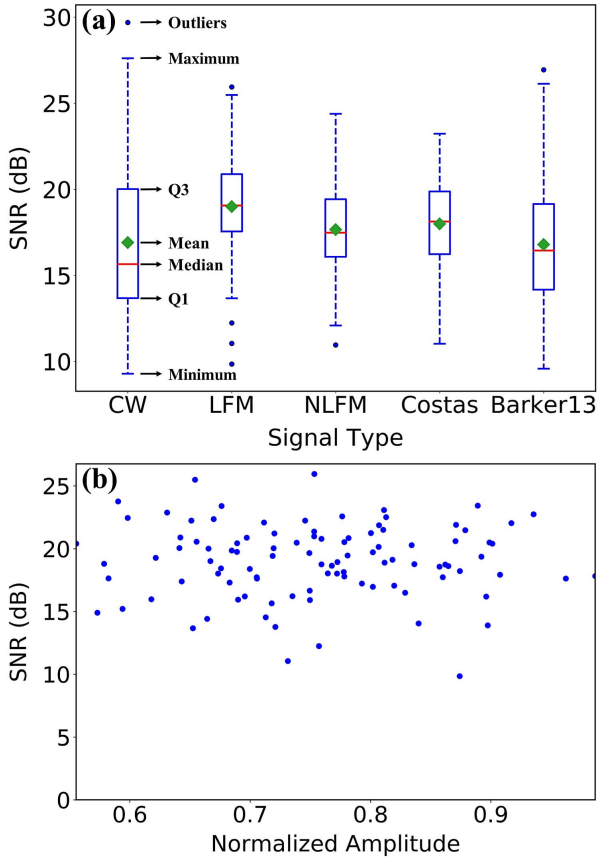

Fig. 4. Experimental results. (a) The box plot of the SNR of different signals reconstructed by DFCN on the test set. Q1, lower quartile; Q3, upper quartile. (b) Separation results of LFM signals at different amplitudes on the test set.

and that a difference in the separation ability for different signals exists in the DFCN, the DFCN can effectively separate ultra-wideband mixed signals in most cases. Figure 4(b) shows the separation results of LFM signals at different amplitudes on the test set. As the amplitude of the signal grows (namely the increase in modulation depth), the SNR of the signal reconstructed by the DFCN remains at a high level. The immunity to nonlinear effects is attributed to the fact that the training set covers mixed signals of different amplitudes. Therefore, the trained DFCN can adapt to the changes in signal amplitude, which ensures the performance of the system.

Furthermore, we implement the signal separation for digitally modulated signals to quantitively verify the effectiveness and performance improvement of the proposed method. In the experiment, the carrier frequency is set to 2.5 GHz, and the type of modulation is binary phase shift keying (BPSK). The transmission bit rate is set to 250 Mb/s, and the bit information inside is completely randomly generated. Here, two antennas are adopted to transmit the digitally modulated signals and the interference signals. The digital signal is transmitted by a TA (TA2, A-INFO LB-340-15-C-SF; frequency range, 2.2–3.3 GHz). TA1 is used to transmit the microwave signal mentioned previously as interference source. The rest of the procedure is the same as the experiments performed earlier. We calculate the average BER before and after the network separation, respectively. Performance evaluation results are shown in Fig. 5. The blue line presents the average BER on the test set without DFCN separation. Due to the interference signals and inherent flaws of the PADC, the average BER is as high as 30.63%. The red and green lines represent the average BER on the training and test sets, respectively. Obviously, it can be seen that before and after DFCN separation, the average BER has been improved by about three orders of magnitude.

In conclusion, we have experimentally demonstrated the ultra-wideband signal acquisition based on a channel-interleaved PADC and a DFCN. We use a channel-interleaved PADC to achieve the reception of ultra-wideband signals. In order to alleviate the interference among wideband signals, we consider the mixed signals as a combination of the target signal and the interference. Then, the DFCN is used to realize the separation of wideband mixed signals, which greatly reduces the influence of interference on the target signal. Furthermore, this is completely an end-to-end mapping, which can save us a lot of tedious operations while ensuring high signal quality. Finally, to quantitatively compare the performance before and after separation, we implement signal separation for digitally modulated signals. The experimental results show that the average BER has been improved by about three orders of magnitude. We believe this work promotes the application of channel-interleaved PADC in modern information systems.

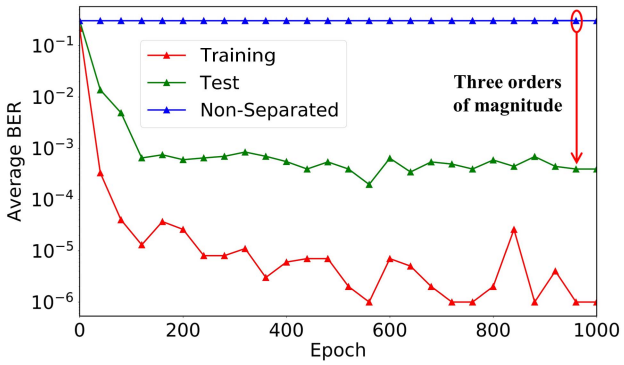

Fig. 5. Experimental results: average BER calculation at different epochs.

This work was supported by the National Key R&D Program of China (No. 2019YFB2203700) and the National Natural Science Foundation of China (Nos. 61822508 and 61571292).

References

1. A. E. Spezio, IEEE Trans. Microwave Theory Tech. **50**, 633 (2002).
2. S. Mehrdad, IEEE Signal Process. Mag. **12**, 21 (1995).
3. G. C. Valley, Opt. Express **15**, 1955 (2007).
4. P. Ghelfi, F. Laghezza, F. Scotti, G. Serafino, A. Capria, S. Pinna, D. Onori, C. Porzi, M. Scaffardi, A. Malacarne, V. Vercesi, E. Lazzeri, F. Berizzi, and A. Bogoni, Nature **507**, 341 (2014).
5. S. Xu, W. Zou, G. Yang, and J. Chen, Chin. Opt. Lett. **16**, 062801 (2018).
6. G. Yang, W. Zou, Y. Yuan, and J. Chen, Chin. Opt. Lett. **16**, 030601 (2018).
7. A. Khilo, S. J. Spector, M. E. Grein, A. H. Nejadmalayeri, C. W. Holzwarth, M. Y. Sander, M. S. Dahlem, M. Y. Peng, M. W. Geis, N. A. DiLello, J. U. Yoon, A. Motamedi, J. S. Orcutt, J. P. Wang, C. M. Sorace-Agaskar, M. A. Popović, J. Sun, G. R. Zhou, H. Byun, J. Chen, J. L. Hoyt, H. I. Smith, R. J. Ram, M. Perrott, T. M. Lyszczarz, E. P. Ippen, and F. X. Kärtner, Opt. Express **20**, 4454 (2012).
8. P. W. Juodawlkis, J. C. Twichell, G. E. Betts, J. J. Hargreaves, R. D. Younger, J. L. Wasserman, F. J. O'Donnell, K. G. Ray, and R. C. Williamson, IEEE Trans. Microwave Theory Tech. **49**, 1840 (2001).
9. L. Yu, W. Zou, G. Yang, X. Li, and J. Chen, Chin. Opt. Lett. **16**, 120602 (2018).
10. S. Xu, X. Zou, B. Ma, J. Chen, L. Yu, and W. Zou, Light: Sci. Appl. **8**, 66 (2019).
11. K. Zheng, W. Zou, L. Yu, N. Qian, and J. Chen, Chin. Opt. Lett. **18**, 012502 (2020).
12. F. Yang, W. Zou, L. Yu, S. Xu, and J. Chen, Chin. Opt. Lett. **17**, 040602 (2019).
13. J. R. Hopgood and P. J. W. Rayner, IEEE Trans. Signal Process. **51**, 1739 (2003).
14. G. Tang, G. Luo, W. Zhang, C. Yang, and H. Wang, Sensors **16**, 897 (2016).
15. P. Parathai, W. L. Woo, and S. S. Dlay, J. Acoust. Soc. Am. **137**, EL124 (2015).
16. B. Gao, W. L. Woo, and S. S. Dlay, IEEE Trans. Audio Speech Lang. Process. **19**, 961 (2010).
17. Y. LeCun, Y. Bengio, and G. Hinton, Nature **521**, 436 (2015).
18. L. Gondara, in *2016 IEEE 16th International Conference on Data Mining Workshops (ICDMW)* (2016), p. 241.

19. B. Karanov, M. Chagnon, F. Thouin, T. A. Eriksson, H. Bülow, D. Lavery, and L. Schmalen, J. Lightwave Technol. **36**, 4843 (2018).
20. S. Pascual, A. Bonafonte, and J. Serra, in *Proceedings of the Conference of the International Speech Communication Association* (2017), p. 3642.
21. K. Zhang, W. Zuo, Y. Chen, D. Meng, and L. Zhang, IEEE Trans. Image Process. **26**, 3142 (2017).
22. H. Zhang, C. Fang, X. Xie, Y. Yang, W. Mei, D. Jin, and P. Fei, Biomed. Opt. Express **10**, 1044 (2019).
23. M. Alex, A. Chaware, K. Kim, K. C. Zhou, P. C. Konda, R. Chen, B. Judkewitz, A. Erdmann, B. Kappes, and R. Horstmeyer, Biomed. Opt. Express **10**, 6351 (2019).
24. J. Long, E. Shelhamer, and T. Darrell, in *Proceedings of the IEEE Conference on Computer Vision and Pattern Recognition* (2015), p. 3431.
25. F. Yu and V. Koltun, arXiv:1511.07122 (2016).
26. S. Ioffe and C. Szegedy, in *Proceedings of the 32nd International Conference on Machine Learning* (2015), p. 448.
27. A. Krizhevsky, I. Sutskever, and G. E. Hinton, in *Advances in Neural Information Processing Systems* (2012), p. 1097.
28. Y. Xu, S. Li, X. Xue, X. Xiao, X. Zheng, and B. Zhou, IEEE Photon. J. **11**, 5502009 (2019).
29. G. Yang, W. Zou, L. Yu, K. Wu, and J. Chen, Opt. Express **24**, 24061 (2016).